Editors' Suggestion

Easy-plane dominant stochastic magnetic tunnel junction with synthetic antiferromagnetic layers

Jonathan Z. Sun, Christopher Safranski, Philip Trouilloud, Christopher D'Emic, Pouya Hashemi, and Guohan Hu
IBM T. J. Watson Research Center, Yorktown Heights, New York 10598, USA

(Received 9 June 2023; accepted 3 August 2023; published 15 August 2023)

We experimentally explore a synthetic-antiferromagnetically (SAF) coupled easy-plane stochastic magnetic tunnel junction (EP-SMTJ) for a baseline device behavior assessment. The tunnel conductance fluctuates over time due to magnetoresistance reflecting the superparamagnetic state of the EP-SMTJ's layers. Binary digitizing at its median gives a stochastic bit stream, which is analyzed using the NIST SP800-22r1a test suite. When the tunnel conductance is sampled at different times for producing the binary bit stream, a best bit rate of ~250 Mb/s is seen. If two independently taken bit streams are XORed, the effective bit rate can be > 1 Gb/s, provided that the in-plane anisotropy is small compared to ambient temperature (k_BT_a). The SAF design for both the free and the reference layer allows for a device conductance fluctuation median that is well centered and only weakly voltage-bias dependent. Comparison of experimental observations with a four-moment coupled finite-temperature macrospin model reveals the role of in-plane anisotropy as causing additional telegraphing fluctuations, which is associated with a longer timescale for stochasticity—a behavior that needs to be optimized for high-speed stochastic bit-stream applications.

DOI: 10.1103/PhysRevB.108.064418

I. INTRODUCTION

A magnetic tunnel junction (MTJ), when operating in its superparamagnetic state, is a compact and power-efficient source of physical entropy for computation [1–15]. For these applications, a fluctuation speed matching that of digital circuits, on the order of a nanosecond or less per bit, is sought for. An easy-plane dominant stochastic magnetic tunnel junction (EP-SMTJ) is of special interest, as it could generate nearly white-spectrum [16] random fluctuations up to gigahertz frequencies [9,11,17–20].

The EP-SMTJs utilize an easy-plane anisotropy to force the magnetic moment to fluctuate largely within the thin-film plane. It relies on thermal agitation as its main drive for fluctuating magnetic states and resulting stochastic tunnel magnetoresistance. For uniform stochastic excursion of tunnel magnetoresistance, the EP-SMTJ needs to have its tunnel free layer (FL) and reference layer (RL) fluctuate independently in a low rotational anisotropy environment, with an in-plane rotational energy variance small compared to the operating temperature, k_BT_a (with $T_a \approx 300$ K as the ambient temperature). This level of low in-plane rotational energy variance requires special consideration in junction design, in part because of the sizable dipolar coupling between the FL and RL of the MTJ, which favors an antiparallel alignment, giving rise to a biased mean value of the fluctuating tunnel conductance. This dipolar effect can be minimized if the junction is sufficiently small in diameter (usually well below 20 nm, for example, as suggested in [21]). It can also be compensated for by utilizing a synthetic antiferromagnetically coupled (SAF) structure as one or both of the MTJ's RL and FL.

In this work we report experimental results on one such EP-SMTJ design utilizing a double SAF FL and RL structure. In doing so, we reduce the role of dipolar field affecting the fluctuation median of the tunnel magnetoresistance. We report this design's basic dynamic behavior, and needs for further optimization. To understand experimental observations, we compare measured results with a numerical model of four-macrospin-coupled Landau-Lifshitz-Gilbert-Slonczewski (LLGS) equations simulation with thermal Langevin field. These provide physics understanding as well as insights for design improvements.

II. EXPERIMENT

The devices are made using a process for MTJ-based spin-transfer-torque random access memory. These EP-SMTJs use a FL-RL design with both composed of a SAF-coupled bilayer of ferromagnets. A sample thin-film layer structure can be, for example, from substrate up and in order of RL | FL: ‖ 20 TaN | 20 Pt | 24 $Co_{70}Fe_{30}$ | 5 Co | 3.75 Ru | 5 Co | 23 $(CoFe)_{70}B_{30}$ | 5 $Co_{70}Fe_{30}$ | ~ 10 MgO | 5 $Co_{70}Fe_{30}$ | 6 $(CoFe)_{70}B_{30}$ | 5 Co | 8 Ru | 5 Co | 6 $(CoFe)_{70}B_{30}$ | ~ 5 MgO | 20 Ta | 200 Ru ‖. Numbers are film thicknesses in Å.

We start the device characterization by examining its quasistatic transport behaviors. The methodology of characterization was described in more detail in Ref. [22].

Similar to simple ferromagnetic FL junctions in Ref. [22], these double SAF FL-RL junctions also show a variety of junction resistance vs bias-voltage (RV) behavior, likely related to an uncontrolled in-plane anisotropy, as discussed in Ref. [22] and further below. One example of two nominally identical junctions, about 35 nm in diameter, and 200 µm apart on the test structure, is shown in Fig. 1. Device A shows relatively weak bias-voltage dependence on junction R_{dc}, whereas device B has stronger bias dependence, and a hint of the so-called 'sigmoidal" response [4,5,23], with high resistance at negative bias indicating a move towards antiparallel of its mean value, and the lower resistance value in positive bias region for a more parallel alignment.

 ©2023 American Physical Society

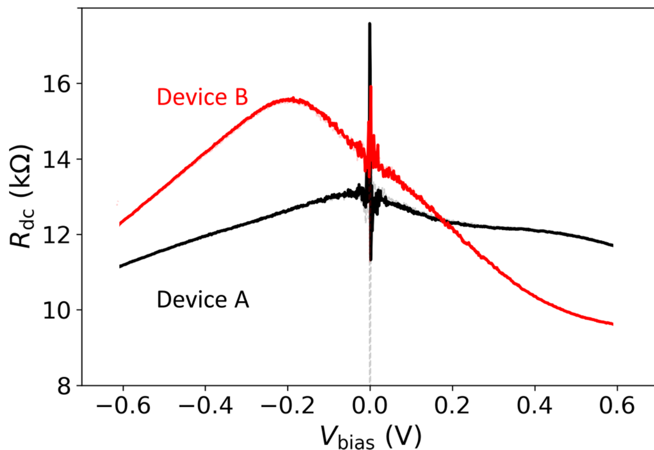

FIG. 1. Two nominally same SAF-based EP-SMTJ's *R-V* characteristics; one (device A) showing weaker bias dependence without the so-called sigmoidal-like transition near zero bias between its P (parallel) and AP (antiparallel) states; while the other (device B) shows stronger bias dependence, and a sigmoidal-like transition. Throughout this paper, we use the polarity convention that $+V$ corresponds to electrons tunneling from RL into FL. Here as in Ref. [22], $R_{dc} = V/I$.

We show below that our circumstantial evidences point to the main difference between such devices A and B as being the absence and presence of an (unintended) in-plane anisotropy of both the FL and the RL. The details of these in-plane anisotropies are not quantitatively known. Indeed, the reduction of such unintended in-plane magnetic anisotropy [22] is a key factor yet to be optimized. This in our process likely results from uncontrolled in-plane strain field on the EP-SMTJ, which couples through magnetostriction to give rise to anisotropy.

This conclusion is based on circumstantial experimental evidences including EP-SMTJ's resistance vs magnetic field sweeps, the relative 'sigmoidal-like" transition widths variation, and the absence or presence of visible "telegraphic" dynamics in high-bandwidth tunnel conductance vs time measurements. This diagnosis is further supported by a four-moment-coupled macrospin simulation with LLGS equations including finite-temperature Langevin fields that describe such SAF FL-RL combination, which will be discussed in more detail in Sec. V. Briefly here, from such simulation with small in-plane anisotropy, one expects a wide range of dampinglike spin-torque bias (corresponding to a wide range of voltage bias on the EP-SMTJ) to result in only small shifts in the mean relative position of the FL and RL, hence only a small dependence of tunnel conductance on bias voltage. This is similar to device A's behavior in Fig. 1. It is also similar to what was reported in a simulation of tunnel junctions with symmetric *ferromagnetic* electrodes in small size limit and at large spin-torque bias [21]. It can be related to the pinwheel-like spin-torque action on both interfaces of a magnetic tunnel junction [24–33], here combined with thermal agitation at finite temperature. When one introduces to simulation an in-plane uniaxial anisotropy on par with $k_B T_a$ the thermal agitation energy, the EP-SMTJ's tunnel conductance STT-bias dependence becomes sharper, and a more sigmoidal-like tunnel conductance response results, resembling the case of device B in Fig. 1.

Following the methodology described in Ref. [22], we next examine the quasistatic behavior of these two device's $R_{dc}(H)$ (*RH*) dependence on magnetic field sweep in Fig. 2, where a full in-plane applied field angular dependence is presented. For these two devices with the film stack described above, both FL and RL are magnetically free to rotate without pinning.[1] The main *RH* peaks in Fig. 2 reflect the scale of SAF exchange-coupling strength. The low-field features represent the FL-RL combined SAF rotational response to the applied field. Details of such rotation are complex as there are four ferromagnetic layers involved, whose in-plane easy-axes directions, SAF exchange coupling, and anisotropy are not known quantitatively. Here we merely point out that (a) the structure is broadly speaking fairly isotropic in-plane especially in the behavior of the main *RH* peak, and (b) there are some distinctions in *low-field behavior* between samples A and B, with sample B involving a larger field scale.[2] This can be gleaned from both the full angular-dependent *RH* sweep traces and in the high-bandwidth measured minor loop *RH* on the rightmost panels of Fig. 2.

III. MEASURING THE EP-SMTJ'S STOCHASTIC FLUCTUATION

The two devices depicted above are measured for their stochastic fluctuation at a static voltage bias, as described in [22]. Some examples of their conductance fluctuation are shown in Fig. 3. For device A, the fluctuation is relatively uniform in excursion, with no apparent low-frequency features in the power spectrum. For device B, a more telegraphic two-state excursion is seen at lower frequencies, as illustrated both by the time traces' apparent telegraphing events, and by the power spectrum's appearance of a lower-frequency plateau. This likely originates from a higher in-plane uniaxial-like anisotropy of device B encouraging a bistable state occupation.

These fluctuation excursion characteristics can also be seen by examining the time trace's state-occupancy statistics, as shown in Figs. 3(c) and 3(g) and with bias dependence in Fig. 4. Device A shows a conductance fluctuation distribution relatively insensitive to bias condition, while device B has a clear bistable concentration, whose occupation probability is narrower, and changes depending on bias condition. As expected, this STT-bias dependent mean conductance change, associated with occupation probability change of the bistable conductance states is what gave device B the stronger bias-voltage dependence, and its sigmoidal-like characteristics in quasistatic *RV* as seen in Fig. 1. The finite width of the bistable

[1]Same as discussed in Ref. [22], we choose *not* to antiferromagnetically pin the RL here but allow it to freely rotate—primarily for processing compatibility with our existing MRAM fabrication route, and also for simpler modeling of noise characteristics. The same considerations would also exist for technology applications.

[2]This is in reference to the behaviors below 500 Oe, not to be confused with the slope of *RH* rise which gives device A a larger field scale.

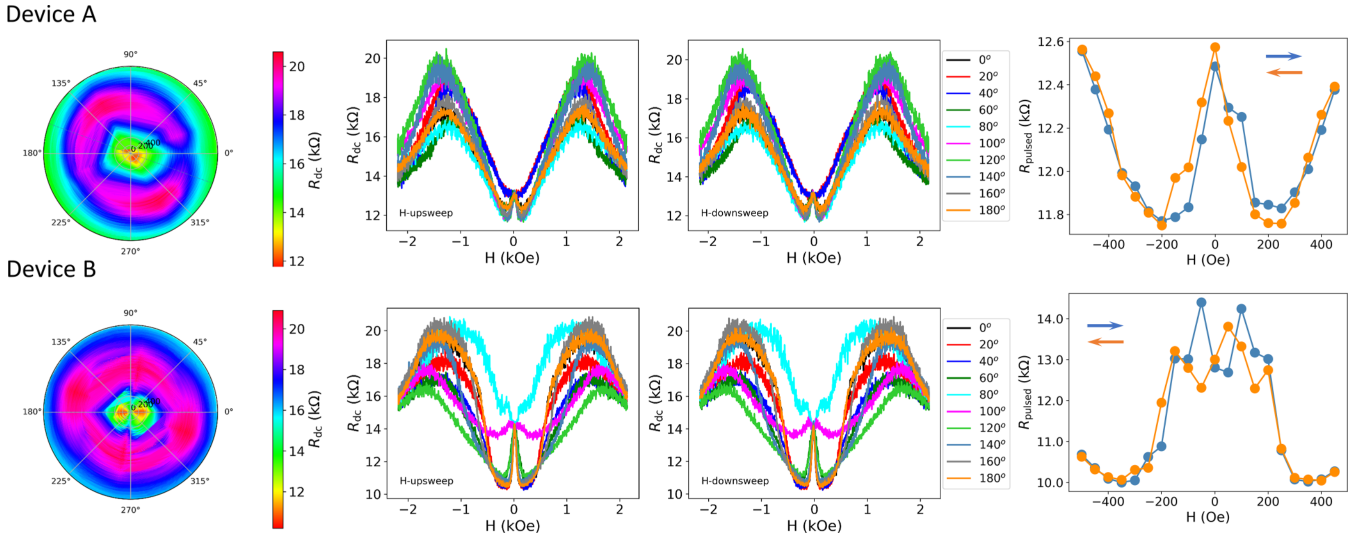

FIG. 2. The *R-H* dependence of devices A (top row) and B (bottom row). For each row, from left to right: *RH* vs field sweeping direction angle (in-plane) contour plot, and line plots for up and down sweep; *RH* along field direction $\theta = 0$ and with high-bandwidth [22] *RH* pulse measured at −0.2 V, 200 ns. The quasi static *RH* were measured at +50 mV voltage bias across the MTJ.

state distribution, particularly visible in Figs. 4(c) and 4(d), is in part also due to measurement circuit noise from the current measurements [22], which in conductance terms tend to increase in magnitude, as the net SMTJ-related fluctuation becomes a smaller part of the total measured current fluctuation. In addition to the EP-SMTJ's stochastic excursion statistics, a general shift towards higher conductance is also present upon higher bias-voltage magnitude, consistent with a bias-dependent tunnel conductance increase related to increased inelastic processes [35].

IV. MEASURING STOCHASTICITY VS SAMPLING TIME: THE EP-SMTJ'S RANDOM BIT RATE

We use the NIST SP800-22r1a stochastic test suite (NIST-STS) [36] for quantifying the randomness of our SMTJ output. NIST-STS is a test suite on stochastic binary bit streams for randomness intended primarily for cryptography. A collection of 188 tests are performed in this experiment, as listed in Fig. 5. Here we use it only as a tool for quantifying bit-stream randomness vs sampling time from our SMTJs,

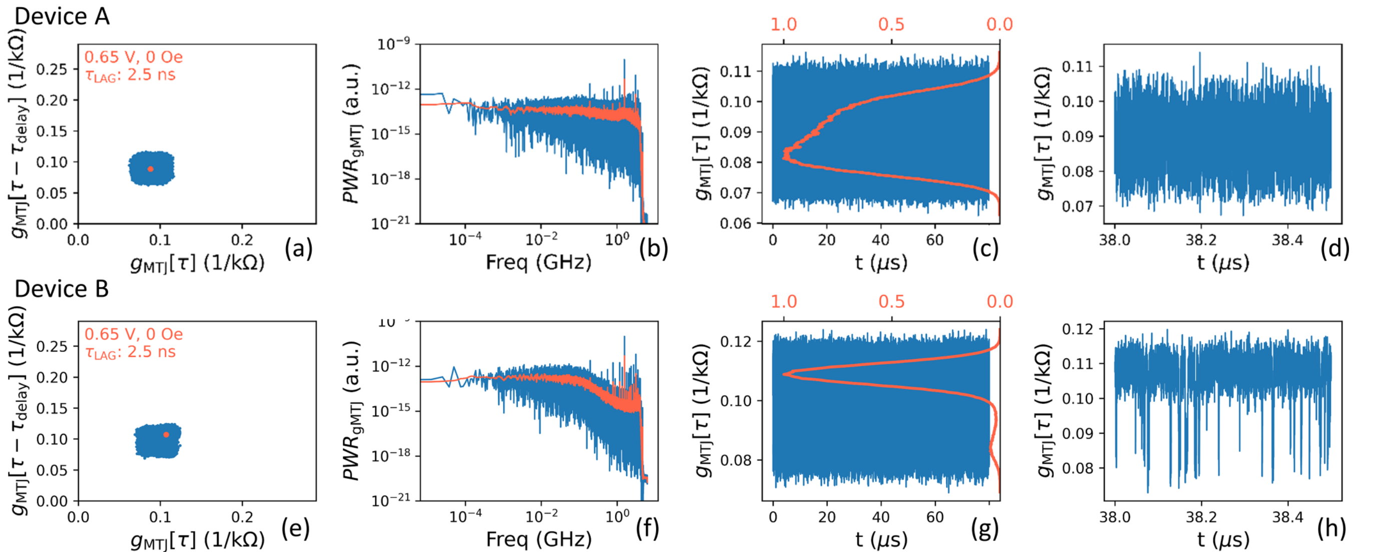

FIG. 3. For device A, (a) a lag plot [34] (by 2.5 ns) of the EP-SMTJ's conductance time dependence, at +0.65 V bias voltage with zero-bias field, with the orange data point showing its median position. (b) Power spectrum of the corresponding time trace. The orange trace is a rolling-averaged representation of the same data. (c) Same data as in (a) but as a time trace for left-*y*, bottom-*x*; left-*y*, top-*x* gives in orange the histogram of the conductance's occupation rate at different values. (d) Same data as in (c), with the time axis expanded in scale to reveal faster motion. (e)–(h) Same measurement data for device B. The cutoff at 4 GHz in (b) and (f) reflects the total measurement bandwidth, limited by the digitization oscilloscope, as discussed in [22]. Data in (c) and (d) and (g) and (h) are the same as in (a) and (e), but auto *y* scaled individually for clearer viewing.

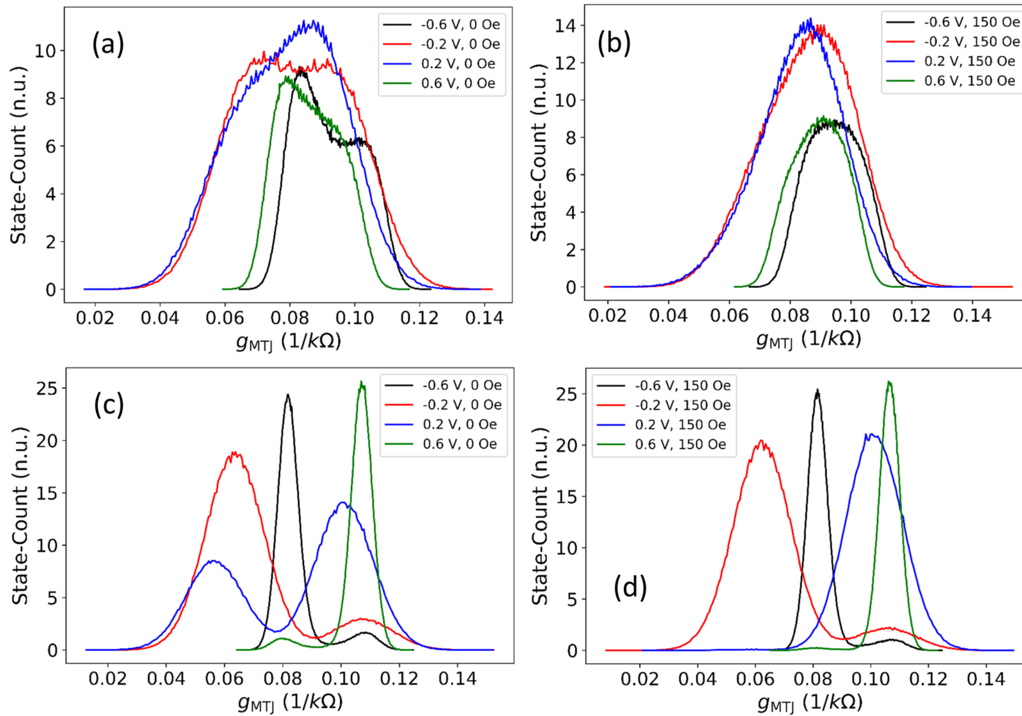

FIG. 4. A closer look at the junction conductance fluctuation's state-occupation histogram at different bias voltage and field for devices A and B. These are histograms obtained on time traces similar to those in Figs. 3(c) and 3(g). (a),(b) Histograms at various field and voltage-bias conditions for device A; (c),(d) for device B.

similar to other works concerned with SMTJs such as in [1]. The analog signal stream in Fig. 3 is binary digitized during time-trace collection, with a discrimination level set at its analog scope record-length median. For signals shown in Fig. 3, the digitizing scope's record length is kept at 80 μs, at 4 GS/s scope sampling speed. The binary digitization sampling time is varied from 0.2 to 8.0 ns on the collected single-trace digital scope output, and without bandwidth reduction. The time-series collection continues until the resulting binary bit stream is filled to 1.5 Mb in length for all sampling times.

Figure 6 presents an example of such NIST-STS test results from the aforementioned devices A and B. Each panel consists of 188 tiled squares, representing the 188 tests shown in Fig. 5, in raster order, from left to right, and from top to bottom. Green indicates passing, orange indicates a "nonoverlapping template" test fail, blue represents an 'approximate entropy" test fail, and red represents all other fails. The digitization sampling time is shown in each test panel. Figure 6 says that generally longer sampling time results in fewer NIST-STS fail counts. In other words, the resulting binary bit stream is more stochastic. Secondly, device A is more stochastic than device B at any given sampling time.

These binary digitization sampling time-dependent behaviors are further summarized in Fig. 7. Here the raw NIST-STS total fail counts as defined in Fig. 6 are shown as a function of sampling time t_{Sample} for several different measurement bias-voltage and field conditions for both devices A and B. For device A, at a $t_{\mathrm{Sample}} = 4$ ns and $V_{\mathrm{bias}} = +0.65$ V, the fail count has decreased to three counts. For device B, while there is a decrease of fail counts at longer t_{Sample}, the level never falls much.

Interestingly, for both devices A and B, there seems to be a minimum t_{Sample} for fail counts (around 4 ns in this set of data). At a larger $t_{\mathrm{Sample}} = 8$ ns, the fail count rises slightly again. This long sampling time end rise behavior is not conclusively understood. It indicates some very long time-base regularity in the digitized bit sequence.[3]

Also worth noting is that by XORing two independently collected bit streams of same measurement condition and length, the fail count vs sampling time behavior is much improved

Total number of tests: 188

Test 1: Frequency
Test 2: Block Frequency
Test 3: Runs
Test 4: Longest Run
Test 5: Rank
Test 6: FFT
Test 7: NonOverlapping Template0
Test 8: NonOverlapping Template1
Test 9: NonOverlapping Template2
…
Test 153: NonOverlapping Template146
Test 154: NonOverlapping Template147
Test 155: Overlapping Template
Test 156: Universal
Test 157: Linear Complexity
Test 158: Serial1
Test 159: Serial2
Test 160: Approximate Entropy
Test 161: CuSum Forward
Test 162: CuSum Backward
Test 163: Random Excursions -4
Test 164: Random Excursions -3
…
Test 169: Random Excursions +3
Test 170: Random Excursions +4
Test 171: Random Excursions Variant -9.0
Test 172: Random Excursions Variant -8.0
…
Test 187: Random Excursions Variant +8.0
Test 188: Random Excursions Variant +9.0

FIG. 5. A list of tests performed using the NIST SP800-22r1a test suite. The test code used is a PYTHON wrapped version [37].

[3]The 1.5 Mb of bits per sampling step length were assembled from multiple 80 μs scope traces as the sampling points ran beyond the single-trace length. This stitching of time series might complicate long time-base measurements, such as small variation of median for every 80 μs segment.

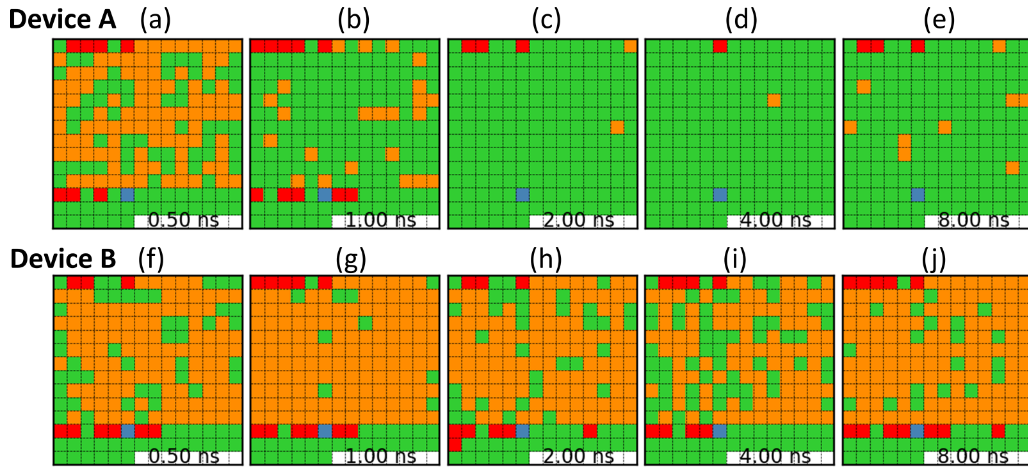

FIG. 6. Results from NIST-STS tests for devices A [(a)–(e)] and B [(f)–(j)]. Each subpanel is a representation of the 188 tests from Fig. 5, tiled in raster order, left to right, top to bottom. Green indicates a pass. Orange is a "nonoverlapping template" fail, blue an "approximate entropy" fail, and red for all other fails—all with default pass-fail criteria as furnished by the PYTHON wrapped code package [37]. White spaces at the end are space fillers with no tests associated. The labels in the white spaces indicate the sampling times for the tests of the panel. Both samples are shown for $V_{\text{bias}} = 0.65$ V and zero applied field.

for device A, while the same XOR procedure does not produce nearly as much improvement for device B. This is illustrated in Figs. 7(b) and 7(d).

As an existence proof, these measurements show that a design of EP-SMTJ with SAF-FL and SAF-RL at selective bias conditions can pass most NIST-STS tests for ∼4 ns sampling time on a single trace, and for < 1 ns sampling time if XORed once. It also demonstrated that the presence of even a small in-plane uniaxial anisotropy could degrade the fluctuation quality and speed significantly. Note that in these measurements we could not separate the measurement circuit's background noise from that of the EP-SMTJ's fluctuation. We do know, however, that the measurement circuit noise alone (taken at $V_{\text{bias}} = 0$) gave very poor fail-count behavior, worse than the lowest finite bias results shown here in Fig. 7. Therefore the actual EP-SMTJ fluctuation itself should have better NIST-STS fail-count performance than shown here, especially for lower-bias voltages. Such operation conditions for the

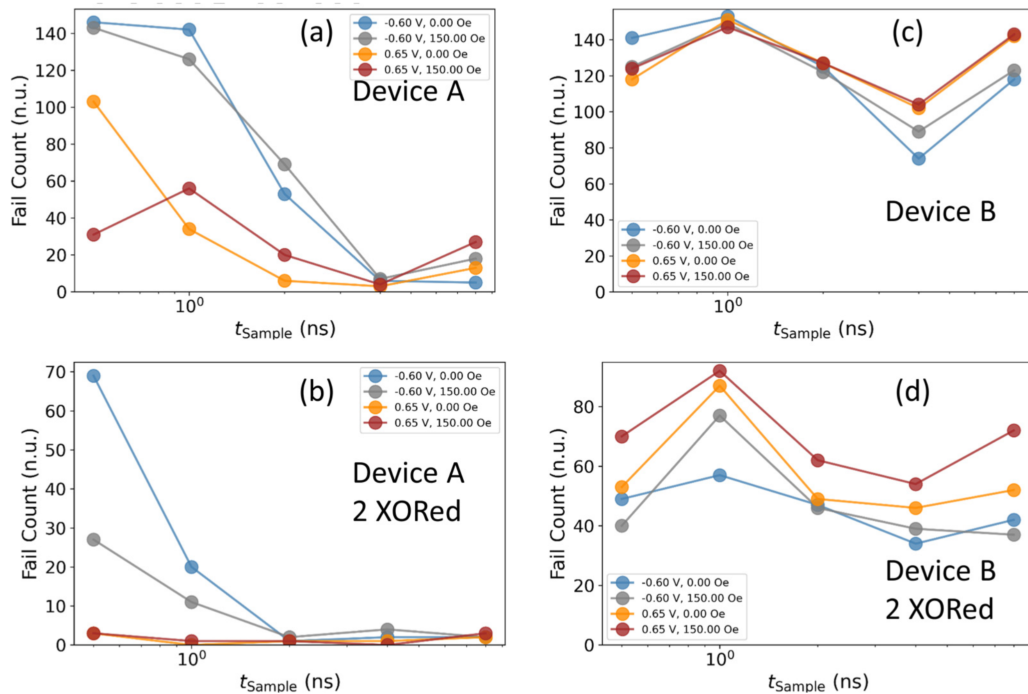

FIG. 7. NIST-STS fail count as shown in Fig. 6 plotted against digitization sampling time. (a) Device A data, counted from Figs. 6(a)–6(e). (b) Device A data, by XORing two passes of identical measurement data—with same parameters and total bit length. (c) Raw fail count vs sampling time for device B, and (d) device B data's XORed results. Four different bias-voltage–applied field combinations were shown here, as indicated by labels in each panel.

EP-SMTJ, however, is not readily accessible with 50 Ω passive measurements, and requires active front-end matching into the tunnel device.

V. COMPARISON WITH NUMERICAL SIMULATION

To understand the materials parameters relationships to the observed SAF-SMTJ behavior, a simple model is developed using a four-macrospin-coupled LLG equation with corresponding thermal agitation Langevin fields, and allowing for all-to-all coupling via both exchange interaction and anti-damping spin-transfer torque. This can be expressed as

$$\begin{aligned}\frac{d\mathbf{n}_{\mathrm{m(u)}}}{dt} - \alpha_{\mathrm{(u)}}\mathbf{n}_{\mathrm{m(u)}} \times \frac{d\mathbf{n}_{\mathrm{m(u)}}}{dt} &= \gamma\Bigg[H_{\mathrm{kz(u)}}(\mathbf{e_z}\cdot\mathbf{n}_{\mathrm{m(u)}})\mathbf{e_z} + H_{\mathrm{kx(u)}}(\mathbf{e_x}\cdot\mathbf{n}_{\mathrm{m(u)}})\mathbf{e_x} \\ &\quad + \sum_{\mathrm{v}=1}^{4}\frac{E_{\mathrm{ex(u,v)}}}{m_{\mathrm{(u)}}}\mathbf{n}_{\mathrm{m(v)}} + \mathbf{H_a} + \mathbf{H}_{\mathrm{L(u)}}\Bigg] \times \mathbf{n}_{\mathrm{m(u)}} \\ &\quad + \mathbf{n}_{\mathrm{m(u)}} \times \left(\mathbf{n}_{\mathrm{m(u)}} \times \sum_{\mathrm{v}=1}^{4} I_{\mathrm{s(u,v)}}\mathbf{n}_{\mathrm{m(v)}}\right), \end{aligned} \tag{1}$$

where integers $(\mathrm{u},\mathrm{v}) \in [1,4]$ label the four moments, and $\mathbf{n}_{\mathrm{m(u)}} = \mathbf{m}_{\mathrm{(u)}}/m_{\mathrm{(u)}}$ are the unit vectors associated with the four moments. Materials parameters describing each moment have a subscript of u or v. H_{kz} represent the out-of-film-plane anisotropy. In this model we have easy-plane anisotropy primarily induced by demagnetization, so $H_{\mathrm{kz(u)}} \approx -4\pi M_{\mathrm{s(u)}}$, with $M_{\mathrm{s(u)}}$ being the layer's saturation magnetization. In addition to the strong easy-plane anisotropy, we also include an orthogonal, in-plane easy-axis anisotropy $H_{\mathrm{kx(u)}}$ for the layers. $\mathbf{e}_{\mathrm{x,y,z}}$ are unit vectors for a Cartesian coordinate system, with z direction being the film norm. The exchange energy between any of the two layers are written here as, for $\mathrm{u} \neq \mathrm{v}$, $E_{\mathrm{ex(u,v)}} = E_{\mathrm{ex(v,u)}} = H_{\mathrm{ex(u,v)}}m_{\mathrm{(v)}} = H_{\mathrm{ex(v,u)}}m_{\mathrm{(u)}}$ with H_{ex} as the corresponding exchange field, $m_{\mathrm{(u)}} = (\pi/4)a^2 t_{\mathrm{(u)}}M_{\mathrm{s(u)}}$ as the u-th layer's total moment, and $t_{\mathrm{(u)}}$ as its corresponding layer thickness, assuming a vertical cylindrical cross section with a uniform diameter a. These geometrical descriptions are only for convenience at estimating the moments. Such macrospin models do not explicitly take into account any shape effects otherwise. Matrix $I_{\mathrm{s(u,v)}}$ describes the possible spin-current coupling among the moments. For practical MTJs, usually only the adjacent layer's $I_{\mathrm{s(u,v)}}$ are nonzero. For low-bias high tunnel magnetization MTJs, $I_{\mathrm{s(u,v)}}$ can also be written in MTJ bias-voltage form, with a linear relationship to the lowest order [38–43]. The Langevin field is written as

$$\mathbf{H}_{\mathrm{L(u)}} = \left[\frac{2\alpha_{\mathrm{(u)}}k_B T}{\left(1+\alpha_{\mathrm{(u)}}^2\right)\gamma m_{\mathrm{(u)}}\Delta t}\right]^{1/2} \sum_{\nu=\mathrm{x,y,z}} R_{\mathrm{n(u,}\nu)}\mathbf{e}_\nu \tag{2}$$

with $R_{\mathrm{n(u,}\nu)}$ as a random Gaussian series at every time step Δt having $\langle R_{\mathrm{n(u,}\nu)}\rangle = 0$ and $\langle R_{\mathrm{n(u,}\nu)}^2\rangle = 1$ for numerical integration. The time integration is done with a fourth-order Runge-Kutta, and checked to be consistent with the Heun-Stratonovich integration scheme for our low damping parameter region [44]. $\gamma = |2\mu_B/\hbar|$ is the magnitude of the gyromagnetic ratio.

Table I is a set of representative parameters used for simulation discussed here. These are parameters generally similar to the film-stack materials design, although not accurately measured specific to our devices. Here the easy-plane anisotropy ξ_{kz} is the full volume anisotropy energy from thin-film demagnetization, without taking into account finite-size effects. The interlayer exchange energies $\xi_{\mathrm{ex(u,v)}} = E_{\mathrm{ex(u,v)}}/k_B T_a$ include two strongly antiparallel couplings between m_1 and m_2, the two forming a SAF FL, and m_3 and m_4 for the reference layer. Other interlayer couplings are either assumed to be zero (for simple model behavior illustrations), or estimates based on the in-plane dipolar field from the given circular shape, of the order of, for example, $H_{\mathrm{ex(1,3)}} \approx \pi^2 M_{\mathrm{s1}}t_1/a$, which is a lowest-order estimate of the in-plane demagnetization field [45,46]. The in-plane uniaxial anisotropy ξ_{kx}'s effect is also illustrated this way below.

An example of the time-integrated "MTJ tunnel conductance" between m_2 and m_3 with and without in-plane uniaxial anisotropy and with no spin current is illustrated in Fig. 8. A time trace of the "tunnel conductance" between m_2 and m_3 shows nearly stochastic excursions, with a state occupation histogram showing some concentration near the parallel and antiparallel boundary, due to the cosine projection of an otherwise even angular distribution. Figure 8(b) is on an expanded time axis of the same, showing more details of the time dependence. These are contrasted with Figs. 8(c) and 8(d), where a small amount ($\sim 1.5 k_B T_a$) of uniaxial anisotropy is assumed for each moment, aligned along $\mathbf{e_x}$. The introduction of this modest in-plane uniaxial anisotropy is seen to cause a telegraphic state to emerge, as seen in the time traces of (c) and (d), as well as a reduced middle state occupation (between P and AP) in the histogram.

The effect of a dampinglike spin torque (i.e., a bias voltage across the MTJ) can be simulated as well. The resulting time trace is averaged to yield a mean value for the tunnel

TABLE I. Parameters used in numerical simulations. $T_a = 300$ K is ambient temperature. "v" variables were varied, as discussed. "bal" (for "balanced") quantities are usually close to 0 unless specifically mentioned in the text. $\xi_{\mathrm{kz(u)}} = m_{\mathrm{(u)}}H_{\mathrm{kz(u)}}/2k_B T_a$ is the reduced easy-plane anisotropy energy. Similarly, $\xi_{\mathrm{kx(u)}}$ is defining an in-plane uniaxial anisotropy. The in-plane anisotropy, if present, is assumed to be uniaxial and along the $\mathbf{e_x}$ direction. Similarly, $\xi_{\mathrm{ex(u,v)}} = E_{\mathrm{ex(u,v)}}/k_B T_a$.

Layer	M_s (emu/cc)	α (n.u.)	t (nm)	ξ_{kz} ($k_B T_a$)	ξ_{kx} ($k_B T_a$)	$\xi_{\mathrm{ex(u,v)}}$ ($k_B T_a$)
1	800	0.01	2.0	−137.3	v	(12): −158.0
2	812	0.01	1.9	−134.4	v	(13,14,23,24): bal
3	800	0.012	2.3	−157.9	v	(32,31,42,41): bal
4	813	0.012	2.1	−148.9	v	(34): −218.6

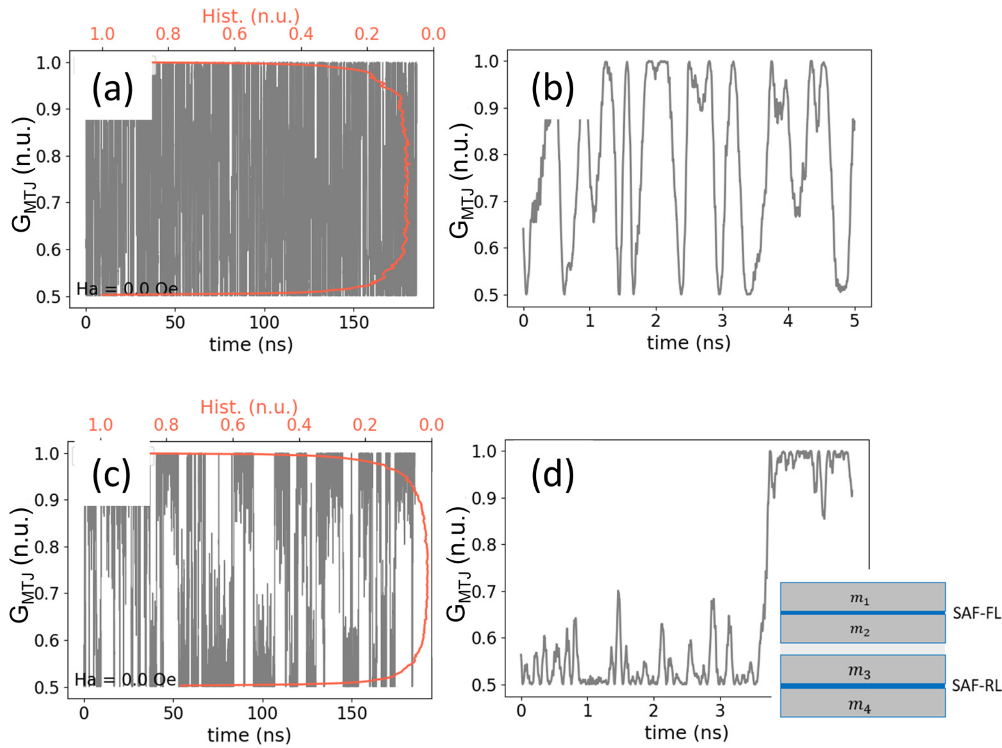

FIG. 8. Time traces of simulated tunnel conductance from model Eq. (1). (a) Tunnel conductance $G_{\rm MTJ} = 1/2 + (1 + \mathbf{n}_{\rm m(2)} \cdot \mathbf{n}_{\rm m(3)})/4$, which assumes a conductance of 0.5 when antiparallel and 1.0 when parallel here for illustration purposes. Orange trace shows a state-occupation histogram along the $G_{\rm MTJ}$ axis. (b) Same as in (a) but with expanded time axis. Simulation for (a) and (b) is without in-plane anisotropy for any of the moments. (c) and (d) are the same quantities as (a) and (b) but run with an in-plane uniaxial anisotropy of $\sim 1.5k_BT_a$ for each of m_1–m_4, along an easy axis in the $\mathbf{e_x}$ direction. The inset of (d) illustrates the layer designation.

conductance $G_{\rm MTJ}$ as defined in Fig. 8 as a function of the biasing spin current between m_2 and m_3. This is illustrated in Fig. 9. The mean conductance here is shown to only weakly depend on spin-current bias for small in-plane anisotropy values, and the effect of in-plane uniaxial anisotropy is seen here to sharpen the low-bias region rise of mean conductance, if a similar amount of in-plane anisotropy is present for both FL and RL, as shown in Fig. 9(a). This is similar to what is seen in experimental data of sample B as compared to sample A. When only one of the FL or RL has a sizable in-plane anisotropy while the other does not, the MTJ conductance tends to be much weaker in its spin-current bias dependence [Fig. 9(b)].

To examine the stochasticity of these time traces we applied the same methodology as for experimental data, of using the NIST-STS test suite. The time-trace integration continues until a 1.5-Mb-long binary bit stream is filled for the given sampling time $t_{\rm Sample}$ just as done in experiment. The results are shown in Fig. 10. Here one sees the fail counts drop to near zero for sampling times longer than 0.4 ns when there is no in-plane easy-axis anisotropy. But the fail count persists to longer sampling time when there is. The fail-count-near-zero sampling time becomes longer for larger in-plane uniaxial anisotropy, reaching 6 ns for $\xi_{\rm IP} \sim 1.57k_BT_a$, the condition similar to data shown in Figs. 8(c) and 8(d). This is sensible, as the telegraphing processes seen in Figs. 8(c) and 8(d) introduce another timescale that tends to increase with an increasing easy-axis anisotropy barrier [47]. The role of spin-current bias, interestingly, is to speed up such telegraphing fluctuations, and to correspondingly reduce the sampling time for NIST-STS fail-count reduction towards zero, as shown in Fig. 10(b), and is also consistent with our experimental observations.

VI. SUMMARY

We demonstrate the fluctuation characteristics of a nanostructured EP-SMTJ using a SAF-FL together with an unpinned SAF-RL. Tunnel conductance fluctuation is seen, and is likely bounded by the SMTJ's P and AP alignment, as illustrated by its time-series lag plots. The fluctuating tunnel conductance has a mean value that could either be weakly or strongly dependent on SMTJ bias voltage. Circumstantial evidence points to the different bias dependences being caused by the presence or absence of an unintended in-plane uniaxial anisotropy, perhaps due to stress field coupled via SMTJ film's magnetostriction.

The analog tunnel conductance fluctuation time trace is binary digitized at its median value, with a varying sampling time distance, and its resulting digital bit stream is examined using the NIST-STS for its stochasticity. The NIST-STS fail count out of a total of 188 tests is used as a gauge for the sampling time at which the binary digitized bit stream assumes a randomness passing the NIST-STS criteria. The fail count generally decreases with increased sampling time. The sampling-based bit stream is seen to a yield fail count below five for sampling times around 4 ns in single-pass measurements, and falls below 5 for 1 ns or less of sampling time

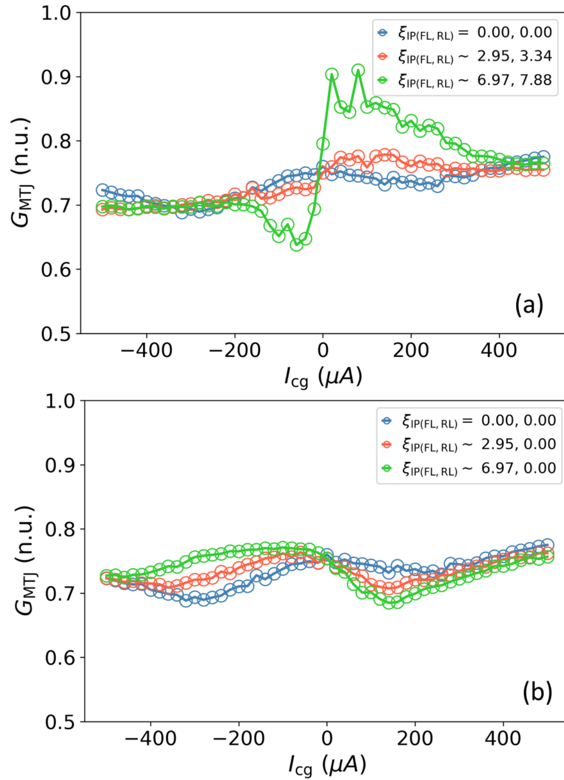

FIG. 9. The simulated STT-bias dependence of mean tunnel conductance G_{total} at various in-plane uniaxial anisotropy values. The tunnel conductance is the time-trace average of that defined in Fig. 8. The bias spin current, in charge-current units (i.e., replacing $\hbar/2$ by electron charge e), is I_{cg}. (a) With FL and RL having $\xi_{\text{IP(FL)}} \lesssim \xi_{\text{IP(RL)}}$; (b) with only FL assuming ξ_{IP}, RL stays without in-plane anisotropy. Here $\xi_{\text{IP(FL,RL)}}$ stands for the FL and RL anisotropy, i.e., $\xi_{\text{IP(FL)}} = \xi_{\text{IP(1)}} + \xi_{\text{IP(2)}}$, and same for $\xi_{\text{IP(RL)}}$. The spin-current thresholds of antidamping instability for individual layers in this parameter set are around 18 μA.

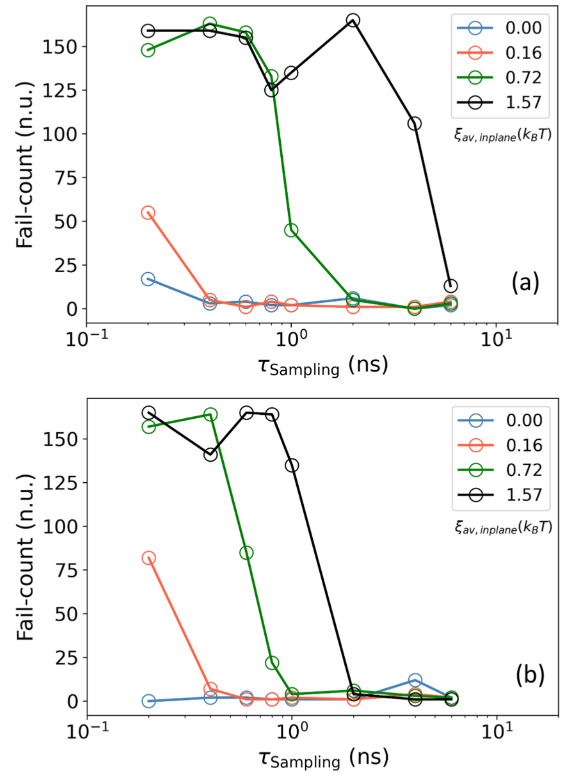

FIG. 10. The corresponding NIST-STS fail count from simulated time traces similar to Fig. 8. (a) With no spin-current bias. (b) At a spin-current bias of 100 μA. The legend labels the approximate in-plane anisotropy ξ_{kx} in $k_B T_a$ for *each layer* $m_{1\text{–}4}$ as defined in Table I.

when XORed once with two independent bit streams taken at +0.65 V bias from the same device. These represent true-random-number bit rates around 250 Mb/s for a single trace, and > 1 Gb/s for two traces XORed, respectively. Fluctuation characteristics at sampling times longer than 8 ns need to be further examined.

A four-moment coupled macrospin model with finite-temperature Langevin field could semiquantitatively describe the observed SAF-FL/SAF-RL SMTJ behavior. The salient features of such systems include (1) a spin-toruqe-bias insensitive mean value, if the FL and RL are nearly symmetric in materials parameters, and are nearly balanced in their dipolar coupling across the tunnel barrier; (2) a stochastic fluctuation that has its minimum timescale as probed by NIST-STS randomness fail count vs sampling time to be around or below 1 ns; (3) the emergence of telegraphinglike fluctuations if additional in-plane easy-axis anisotropy is introduced, which can significantly increase the fluctuation's timescale for randomness; and (4) the additional in-plane easy-axis anisotropy, if introduced in both FL and RL with comparable magnitudes, would result in an increase in a low spin-current bias region's tunnel conductance vs bias dependence, and cause an appearance of a junction *RV* resembling the so-called sigmoidal characteristics [5], although usually not achieving full P or AP mean values, and reverts to a more intermediate mean value upon further increase of spin-current bias. If one of the FL or RL's ξ_{IP} is much lower than that of the other layer's, the resulting *RV* only varies weakly with STT bias.

ACKNOWLEDGMENTS

Work done with the MRAM group at IBM T. J. Watson Research Center is supported in part by a partnership with Samsung Electronics. We acknowledge the valuable support for these experiments by the IBM Microelectronics Research Lab at Yorktown, and insightful discussions with Daniel Worledge on the statistical analysis of these results.

[1] D. Vodenicarevic, N. Locatelli, A. Mizrahi, J. S. Friedman, A. F. Vincent, M. Romera, A. Fukushima, K. Yakushiji, H. Kubota, S. Yuasa, S. Tiwari, J. Grollier, and D. Querlioz, Phys. Rev. Appl. **8**, 054045 (2017).

[2] J. Grollier, D. Querlioz, and M. D. Stiles, Proc. IEEE **104**, 2024 (2016).

[3] J. Torrejon, M. Riou, F. A. Araujo, S. Tsunegi, G. Khalsa, D. Querlioz, P. Bortolotti, V. Cros, K. Yakushiji, A. Fukushima, H. Kubota, S. Yuasa, M. D. Stiles, and J. Grollier, Nature (London) **547**, 428 (2017).

[4] B. Sutton, K. Y. Camsari, B. Behin-Aein, and S. Datta, Sci. Rep. **7**, 44370 (2016).

[5] K. Y. Camsari, R. Faria, B. M. Sutton, and S. Datta, Phys. Rev. X **7**, 031014 (2017).

[6] K. Y. Camsari, S. Chowdhury, and S. Datta, Phys. Rev. Appl. **12**, 034061 (2019).

[7] K. Y. Camsari, S. Salahuddin, and S. Datta, IEEE Electron Device Lett. **38**, 1767 (2017).

[8] K. Y. Camsari, B. M. Sutton, and S. Datta, Appl. Phys. Rev. **6**, 011305 (2019).

[9] O. Hassan, R. Faria, K. Y. Camsari, J. Z. Sun, and S. Datta, IEEE Magn. Lett. **10**, 4502805 (2019).

[10] W. A. Borders, A. Z. Pervaiz, S. Fukami, K. Y. Camsari, H. Ohno, and S. Datta, Nature (London) **573**, 390 (2019).

[11] J. Kaiser, A. Rustagi, K. Y. Camsari, J. Z. Sun, S. Datta, and P. Upadhyaya, Phys. Rev. Appl. **12**, 054056 (2019).

[12] J. Kaiser, R. Faria, K. Y. Camsari, and S. Datta, Front. Comput. Neurosci. **14**, 1 (2020).

[13] J. Kaiser, W. A. Borders, K. Y. Camsari, S. Fukami, H. Ohno, and S. Datta, Phys. Rev. Appl. **17**, 014016 (2022).

[14] R. Faria, J. Kaiser, K. Y. Camsari, and S. Datta, Front. Comput. Neurosci. **15**, 584797 (2021).

[15] A. Alaghi and J. P. Hayes, ACM Trans. Embed. Comput. Syst. **12**, 1 (2013).

[16] C. Aron, D. G. Barci, L. F. Cugliandolo, Z. G. Arenas, and G. S. Lozano, J. Stat. Mech. (2014) P09008.

[17] B. Sutton, R. Faria, L. A. Ghantasala, R. Jaiswal, K. Y. Camsari, and S. Datta, IEEE Access **8**, 157238 (2020).

[18] K. Kobayashi, W. A. Borders, S. Kanai, K. Hayakawa, H. Ohno, and S. Fukami, Appl. Phys. Lett. **119**, 132406 (2021).

[19] S. Kanai, K. Hayakawa, H. Ohno, and S. Fukami, Phys. Rev. B **103**, 094423 (2021).

[20] C. Safranski, J. Kaiser, P. Trouilloud, P. Hashemi, G. Hu, and J. Z. Sun, Nano Lett. **21**, 2040 (2021).

[21] K. Y. Camsari, M. M. Torunbalci, W. A. Borders, H. Ohno, and S. Fukami, Phys. Rev. Appl. **15**, 044049 (2021).

[22] J. Z. Sun, C. Safranski, P. Trouilloud, C. D'Emic, P. Hashemi, and G. Hu (unpublished).

[23] Y. Shim, A. Jaiswal, and K. Roy, J. Appl. Phys. **121**, 193902 (2017).

[24] Y. B. Bazaliy, D. Olaosebikan, and B. A. Jones, J. Nanosci. Nanotechnol. **8**, 2891 (2008).

[25] Ya. B. Bazaliy, arXiv:0710.2564.

[26] M. Tsoi, J. Z. Sun, and S. S. P. Parkin, Phys. Rev. Lett. **93**, 036602 (2004).

[27] J. C. Slonczewski, Phys. Rev. B **39**, 6995 (1989).

[28] J. Slonczewski, Theory of spin-polarized current and spintransfer torque in magnetic multilayers, in *Handbook of Magnetism and Advanced Magnetic Materials, Spintronics and Magnetoelectronics*, edited by H. Kronmüller and S. Parkin (John Wiley & Sons, Ltd., New York, 2007), Vol. 5, p. 2648.

[29] T. Min, J. Z. Sun, R. Beach, D. Tang, and P. Wang, J. Appl. Phys. **105**, 07D126 (2009).

[30] J. Z. Sun, M. C. Gaidis, G. Hu, E. J. O'Sullivan, S. L. B. Nowak, P. L. Trouilloud, and D. C. Worledge, J. Appl. Phys. **105**, 07D109 (2009).

[31] W. Kim, T. D. Lee, and K.-J. Lee, Appl. Phys. Lett. **93**, 232506 (2008).

[32] C. Safranski and J. Z. Sun, Phys. Rev. B **100**, 014435 (2019).

[33] T. Devolder, O. Bultynck, P. Bouquin, V. D. Nguyen, S. Rao, D. Wan, B. Sorée, I. P. Radu, G. S. Kar, and S. Couet, Phys. Rev. B **102**, 184406 (2020).

[34] For definition, see https://www.itl.nist.gov/div898/handbook/eda/section3/lagplot.htm.

[35] J. Z. Sun, Phys. Rev. B **103**, 094439 (2021).

[36] A. Rukhin, J. Soto, J. Nechvatal, M. Smid, E. Barker, S. Leigh, M. Levenson, M. Vangel, D. Banks, N. Heckert, J. Dray, S. Vo, and L. Bassham, NIST Publications, https://csrc.nist.gov/publications/detail/sp/800-22/rev-1a/final.

[37] T. Moore, https://github.com/terrillmoore/NIST-Statistical-Test-Suite.

[38] J. C. Slonczewski, Phys. Rev. B **71**, 024411 (2005).

[39] J. C. Slonczewski and J. Z. Sun, J. Magn. Magn. Mater. **310**, 169 (2007).

[40] J. Z. Sun and D. C. Ralph, J. Magn. Magn. Mater. **320**, 1227 (2008).

[41] J. Z. Sun, Proc. SPIE **9931**, 993113 (2016).

[42] D. C. Worledge, IEEE Magn. Lett. **8**, 4306505 (2017).

[43] J. Z. Sun, J. Magn. Magn. Mater. **559**, 169479 (2022).

[44] V. P. Antropov, S. V. Tretyakov, and B. N. Harmon, J. Appl. Phys. **81**, 3961 (1997).

[45] J. A. Osborn, Phys. Rev. **67**, 351 (1945).

[46] M. Beleggia, M. D. Graef, Y. T. Millev, D. A. Goode, and G. Rowlands, J. Phys. D: Appl. Phys. **38**, 3333 (2005).

[47] W. F. Brown, Phys. Rev. **130**, 1677 (1963).